Valence Band Splitting in Wurtzite InGaAs Nanoneedles Studied by Photoluminescence Excitation Spectroscopy

Xiaodong Wang,*[†,§] Ilaria Zardo,*[†,⊥] Dančе Spirkoska,[†] Sara Yazji,[†] Kar Wei Ng,[∥] Wai Son Ko,[∥] Connie J. Chang-Hasnain,[∥] Jonathan J. Finley,[†] and Gerhard Abstreiter[†,‡]

[†]Walter Schottky Institut & Physik Department, Technische Universität München, D-85748 Garching, Germany, [§]Shanghai Key Laboratory of Special Artificial Microstructure Materials and Technology & School of Physics Science and Engineering, Tongji University, Shanghai 200092, P. R. China, [⊥]Department of Applied Physics, Eindhoven University of Technology, 5600 MB Eindhoven, The Netherlands, [∥]Department of Electrical Engineering and Computer Sciences & Applied Science and Technology Group, University of California at Berkeley, Berkeley, California 94720, United States, and [‡]Institute for Advanced Study, Technische Universität München, D-85748 Garching, Germany

ABSTRACT We use low-temperature microphotoluminescence and photoluminescence excitation spectroscopy to measure the valence band parameters of single wurtzite InGaAs nanoneedles. The effective indium composition is measured by means of polarization-dependent Raman spectroscopy. We find that the heavy-hole and light-hole splitting is ∼95 meV at 10 K and the Stokes shift is in the range of 35−55 meV. These findings provide important insight in the band structure of wurtzite InGaAs that could be used for future bandgap engineering.

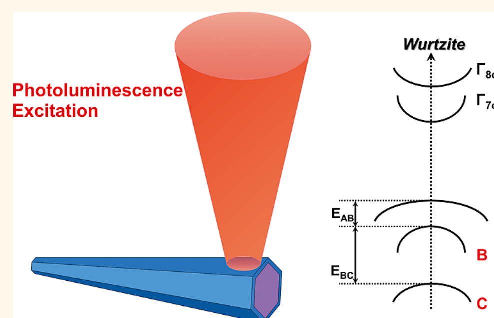

KEYWORDS: InGaAs nanoneedle · wurtzite · band structure · photoluminescence excitation spectroscopy · Raman spectroscopy

It is now well established that nanoscale materials (wire, needle, *etc.*) of III−V semiconductors can be grown in wurtzite (WZ) phase along their length, although the corresponding bulk materials are in zinc-blende (ZB) phase.[1−6] The ability to control the crystal phase of nanoscale semiconductor materials opens up new opportunities for band structure engineering within only a single material. For the design of these novel structures, it is essential to have a clear interpretation of the band structure of the WZ crystal phase.

As a consequence of the change in the crystal symmetry from cubic to hexagonal, the electronic band structure is modified, as schematically shown in Figure 1a. In contrast to ZB phase, the valence band of WZ semiconductors splits in three bands (heavy-hole (A band), light-hole (B band), and crystal-filed-split-off (C band)) as a combination of spin−orbit and crystal field splitting. The recent prediction of bandgap positions and drastic changes in the electronic band structure and optical properties of III−V semiconductors WZ phase[7−10] motivated us to further investigate in detail their physical properties through experiments. Probably the most complete picture has been obtained by optical measurements on WZ InP nanowires, where the band gap energy of the WZ phase has been determined to be 70 meV greater than that of the ZB phase.[11−15]

Ternary InGaAs nanowires (NWs)/nanoneedles (NNs) have attracted tremendous research interest due to high electron mobilities and tunable Schottky barrier heights, widely tunable band gap energies, and emission wavelengths even below the silicon band edge.[16,17] These unique features, therefore, pave the way for next-generation photovoltaics,[18] integrated photonics,[19−21] tunneling devices,[22] and high-performance gate all-round III−V/Si NW transistors.[23] Recently, catalyst-free, self-assembled WZ InGaAs NNs have been grown and reported by Chang-Hasnain's group.[24] So far, numerous

* Address correspondence to xiaodong_wang@tongji.edu.cn, i.zardo@tue.nl.

Received for review August 12, 2014 and accepted November 2, 2014.

Published online November 02, 2014
10.1021/nn504512u

© 2014 American Chemical Society

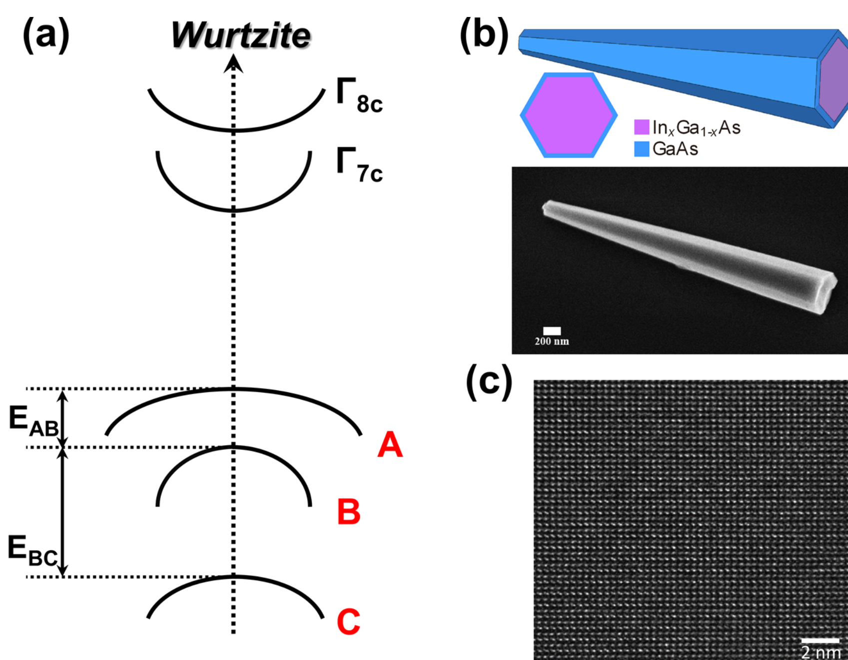

Figure 1. (a) Schematic presentation of the band structure of wurtzite $In_xGa_{1-x}As$. (b) Schematic of the core–shell $In_xGa_{1-x}As$/GaAs NN geometry (upper part) and SEM micrograph of a single $In_{0.2}Ga_{0.8}As$ NN (lower panel). (c) HRTEM image of an $In_{0.2}Ga_{0.8}As$ NN showing the characteristic zigzag lattice of the wurtzite phase crystal.

theoretical and experimental investigations were performed to resolve the band structure in WZ GaAs[25−30] and InAs.[31] For composition-tunable WZ InGaAs NNs/NWs, no investigations have yet been performed to elucidate their band structure parameters.

Photoluminescence excitation (PLE) spectroscopy is a widely used spectroscopic tool to investigate the optical transitions in semiconductors. In particular, PLE has been successfully applied to resolve the valence band structure of WZ InP NWs.[11−13] In this technique, the spectrometer is set to detect emission of a specific photon energy from the sample. The emission intensity is then recorded as a function of the excitation photon energy. It is often assumed that the PLE spectrum is roughly equivalent to the absorption spectrum of the sample.[32] PLE, therefore, has become an alternative for absorption measurements since it is extremely challenging to perform the absorption measurements directly on NW/NN, especially on single NW/NN.

In this paper, we present microphotoluminescence (μ-PL) and microphotoluminescence excitation (μ-PLE) measurements of single WZ InGaAs–GaAs core–shell NNs grown by metal–organic chemical vapor deposition (MOCVD) on silicon substrates. In all samples, a clear Stokes shift (35–55 meV) between the PL peak and the lowest absorption band in the PLE spectrum has been observed. In particular, we resolve the valence band splitting in WZ InGaAs. The PLE results show that the splitting between A and B bands (E_{AB}) is about 95 meV. We expect these results will be used in the future for further bandgap engineering using InGaAs polytypes.

RESULTS AND DISCUSSION

The core–shell NN geometry is schematically depicted in Figure 1b together with a scanning electron microscope (SEM) image. The height and diameter of the NN scale easily and controllably with growth time, despite the large lattice mismatch. Its cross-section reveals inner core–shell layers (see inset for a top view). As shown by the SEM image, the NN displays extremely well-faceted geometry and has a 5° taper between opposite sidewall facets. The NNs are strongly tapered with a typical diameter in the bottom from 600 nm. The structure of the NNs was shown to be single-crystal WZ, free of twinning defects, as shown by the high-resolution transmission electron microscopy (HRTEM) image in Figure 1c.[24]

The effective indium composition was measured by means of Raman spectroscopy. Raman spectra of $In_xGa_{1-x}As$ NNs with different indium composition capped with 30 nm of GaAs are shown in Figure 2a. Spectra were collected under different scattering configurations in order to detect the different phonon modes with different symmetry. Using the so-called Porto notation, the spectra were collected under $\bar{x}(z,z)x$ and $\bar{x}(y,y)x$ scattering configurations, *i.e.*, with the direction of propagation of the incident and analyzed radiation perpendicular to the NN growth axis and the polarization of the incident and analyzed radiation either parallel or perpendicular to the growth axis, respectively. In the $\bar{x}(z,z)x$ configuration only the transversal optical (TO) mode is present, while also the E_2^H mode is present in the $\bar{x}(y,y)x$ scattering configuration. The variation of frequency positions for the various

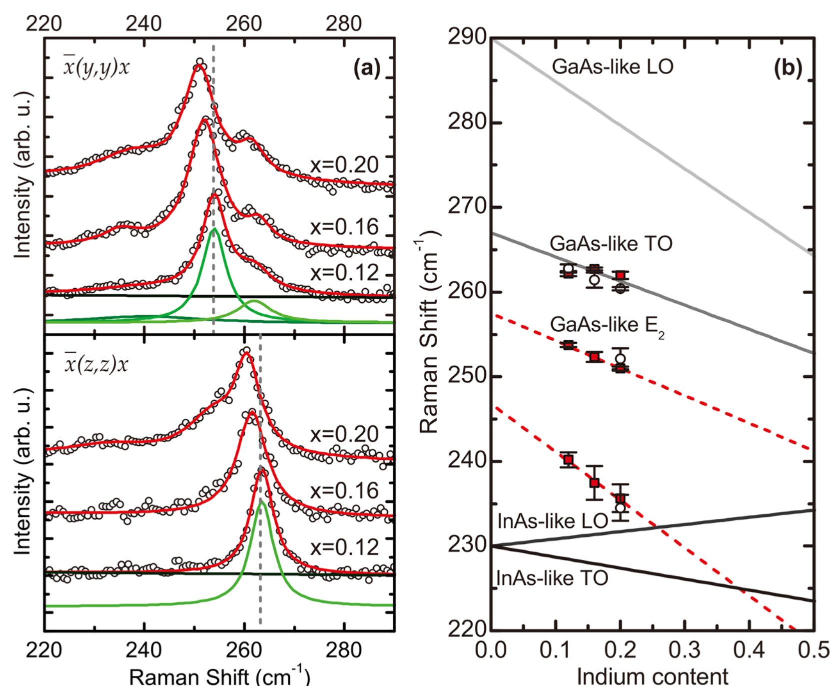

Figure 2. (a) Raman spectra (open symbols) of $In_xGa_{1-x}As$ nanoneedles with different In content (0.12, 0.16, 0.20) capped with 30 nm of GaAs measured under the $\bar{x}(z,z)x$ (bottom panel) and $\bar{x}(y,y)x$ (top panel) scattering configurations. Spectra are normalized to the GaAs-like TO and to GaAs-like E_2^H phonon peaks, respectively, and are shifted for clarity. A multiple-Lorentzian fitting was conducted (solid lines). (b) Variation of frequency positions for various optical phonons with respect to indium composition. Symbols represent experimental data points under the $\bar{x}(z,z)x$ (open symbols) and $\bar{x}(y,y)x$ (filled symbols) scattering configurations. Solid lines indicate theoretical estimations obtained for ZB $In_xGa_{1-x}As$,[33] and dashed lines are linear fit for the GaAs-like E_2^H mode and InAs-like E_2^H.

TABLE 1. Measured Indium Composition, Energies of the Absorption Edges, Stokes Shift, and Their Energy Separation between A and B Bands for the Samples with Different Nominal Indium Composition

indium conc (x)	indium conc determined by Raman	E_A (eV)	E_B (eV)	Stokes shift (meV)	E_{AB} (meV)
0.20	0.22−0.24	1.304 ± 0.008	1.394 ± 0.002	40.3 ± 7.6	90.3 ± 6.8
0.16	0.17−0.22	1.329 ± 0.011	1.417 ± 0.007	46.2 ± 8.3	93.0 ± 3.0
0.12	0.12−0.15	1.382 ± 0.006		52.7 ± 3.4	

optical phonons with respect to indium composition is plotted in Figure 2b. The theoretical estimates obtained for ZB $In_xGa_{1-x}As$ are depicted as solid lines. The effective indium composition of the $In_xGa_{1-x}As$ NNs reported in Table 1 was extracted by the Raman shift of the GaAs-like TO.

The possible presence of composition fluctuations along the NN or strain either due to shell or to the specific shape of the NNs was also investigated by Raman spectroscopy. For this purpose, Raman spectra were collected at different position along the NN (Figure 3a) as well as from NNs with different GaAs shell thickness but the same indium composition (Figure 3b). In both cases, we do not observe any significant variation that could be attributed to the presence of strain or composition fluctuation along the NNs. Notably, the GaAs LO phonon mode at 287 cm^{-1} from the GaAs shell is visible in the measurements performed on the NNs with the thickest shell. This mode is downshifted about 2 cm^{-1} with respect to the bulk counterpart, which could be explained with tensile strain. However, we do not observe a consistent variation in Raman shift of the phonon modes with increasing shell thickness within the shell thickness range investigated. As well, we do not observe an increase in full width at half maximum (FWHM) of the phonon modes. Therefore, while the thicker shell might be strained, we can exclude the presence of strain in the core.

Figure 4a displays a typical power-dependent μ-PL spectra (T = 10 K) for a single WZ $In_xGa_{1-x}As$ NN with x = 0.20. Under a low excitation power (Figure 4b, 0.1 μW), a main emission band centered at 1.267 eV is present, with a weak shoulder at the low energy side which moves gradually to higher energy as the excitation power raises. For high excitation power (Figure 4c, 5 μW), we observe the emergence of an additional emission band at higher energies, at ~1.30 eV. The energy separation between those two emission bands (~33 meV) is compatible with the binding energy of an acceptor impurity in $In_xGa_{1-x}As$.[32,34−37] On the other hand, the main emission band shows a blue shift with increasing excitation powers, which is also expected

for a donor–acceptor recombination.[12,38,39] Therefore, we attribute the main emission band from our NN to a band–acceptor (e–A) and donor–acceptor (D–A) recombination in WZ $In_xGa_{1-x}As$.

In order to ascertain the intrinsic nature of the observed emission, μ-PLE measurements have been performed. μ-PLE measurements on NNs are very sensitive

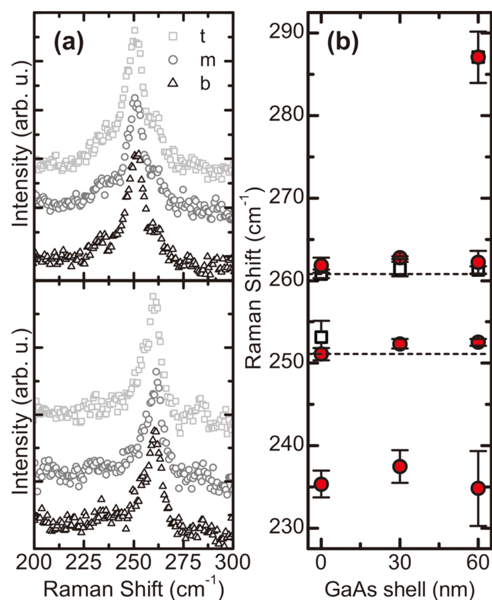

Figure 3. (a) Raman spectra collected from three different positions, top (t), middle (m), and bottom (b), along an uncapped $In_{0.16}Ga_{0.84}As$ measured under the $\bar{x}(z,z)x$ (bottom panel) and $\bar{x}(y,y)x$ (top panel) scattering configurations. The spectra have been normalized to the GaAs-like TO (A_1+E_1) and to the GaAs-like E_2^H modes and are shifted vertically for clarity. (b) Raman shift of the optical phonons of the $In_{0.16}Ga_{0.84}As$ nanoneedle core as a function of GaAs shell thickness. The open symbols represent experimental data points under the $\bar{x}(z,z)x$ scattering configuration and the filled symbols under the $\bar{x}(y,y)x$ scattering configurations. The dashed lines indicate the frequency position of the GaAs-like TO (A_1+E_1) and of the GaAs-like E_2^H modes for uncapped $In_{0.16}Ga_{0.84}As$ nanoneedles.

to the correct alignment; therefore, we took special care in adjusting the correct focus at each different excitation wavelengths. Thus, the PLE scans were done point by point manually rather than in a computerized way. The PLE spectrum shown in Figure 5a was obtained by measuring the intensity of the PL emission at 1.277 eV (indicated with a gray arrow and gray dotted line in the figure). In these measurements, the incident laser had an arbitrary polarization with respect to the NN growth direction, while the emission was collected for all polarizations. We assume here that the hole relaxation from A, B and C valence bands to the acceptor impurity level is faster than its recombination, as expected for bulk materials.[12,32] The PLE spectrum is characterized by a pronounced peak at energy of 1.311 eV and a second plateau whose onset starts at an energy of 1.40 eV. We attribute the first peak to the absorption from the exciton of the A band and the second plateau to the absorption in the B band. Interestingly, for energies above 1.47 eV the emission intensity is decreasing instead of increasing, which makes it impossible to resolve the position of C band. We ascribe this decrease to the absorption in the WZ GaAs shell. As already mentioned, the GaAs shell has also a WZ structure and, therefore, A, B and C subbands in the valence band. Two plateaus located at energies of approximately 1.51 and 1.60 eV can be distinguished in the curve, which most probably comes from the absorption in the A and B subbands in the WZ GaAs. These two positions are consistent with the previous study reported by Ketterer.[25]

The symmetry of the lowest conduction band in WZ III–V semiconductor alloys has been the subject of controversy in the past few years. Knowledge of the conduction band symmetry would have a major impact on the electronic transport and optical properties of WZ materials. It is already known[25,40] that radiative processes between the Γ_7 conduction band and all

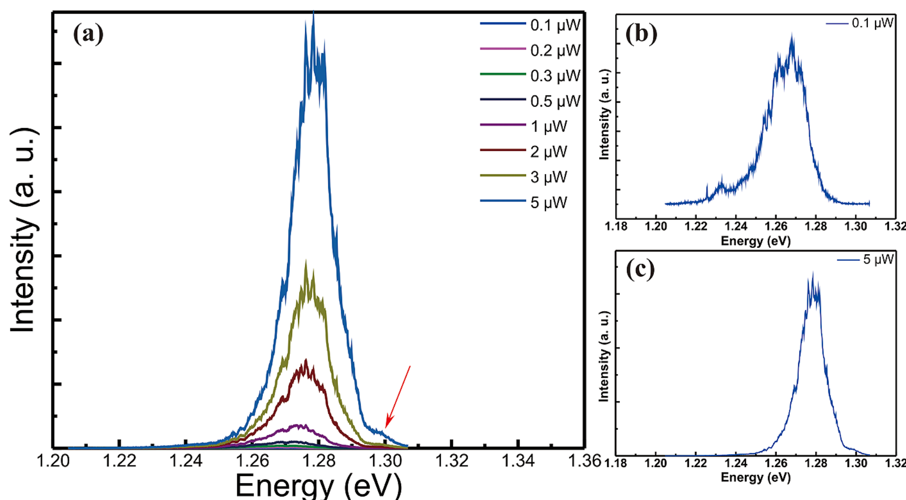

Figure 4. (a) Power-dependent PL spectra for an $In_{0.2}Ga_{0.8}As$ NN. (b) PL spectra of an $In_{0.2}Ga_{0.8}As$ NN at an excitation laser power of 0.1 μW. (c) PL spectra of an $In_{0.2}Ga_{0.8}As$ NN at an excitation laser power of 5 μW.

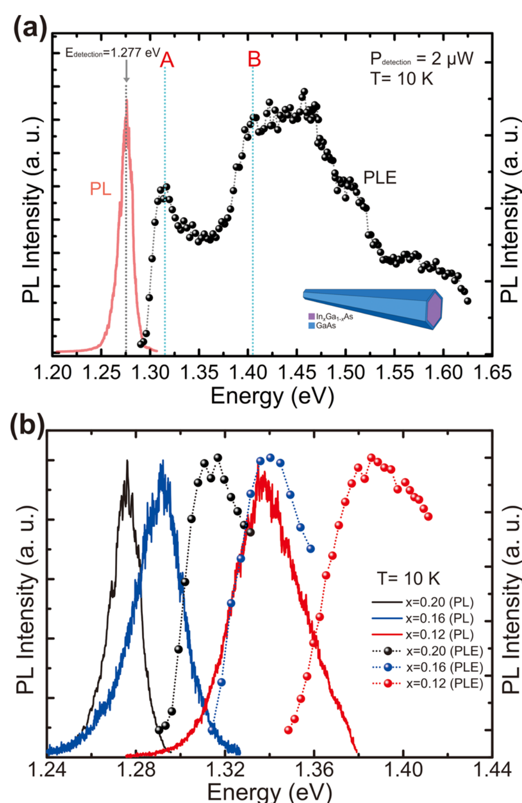

Figure 5. (a) PL (red line) and PLE (black dotted line and symbols) from a single WZ $In_{0.2}Ga_{0.8}As$ NN. The PLE spectrum was obtained by measuring the emitted PL at detection energy of 1.277 eV (indicated with a gray arrow and gray dotted line). (b) PL (solid lines) and PLE spectra (dotted line and symbols) from three distinguished NNs with different indium content (0.20, 0.16, 0.12).

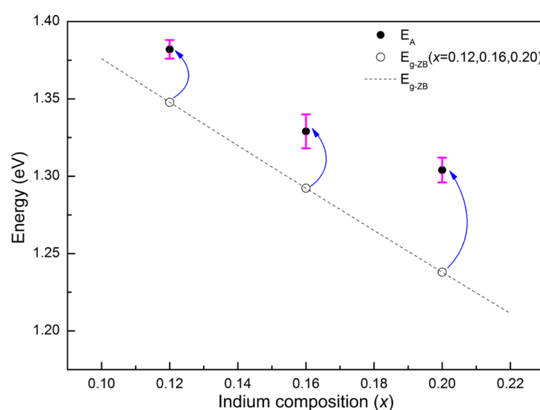

Figure 6. Measured bandgap energy E_A (black filled symbols) of the WZ $In_xGa_{1-x}As$ NN as a function of indium composition x. The expected bandgap energy dependence of ZB $In_xGa_{1-x}As$ (according to ref 41) is shown in dashed line. The corresponding calculated bandgap energy of ZB $In_xGa_{1-x}As$ (x = 0.12, 0.16, 0.20) is also plotted as black open symbols for better comparison.

valence band states are possible. For the Γ_8 conduction band, the transition is only allowed between the Γ_8 conduction band and the heavy-hole state (A band), whereas transitions between the Γ_8 conduction band and the light-hole state (B band) are always forbidden. In our measurements, both the A and B bands in valence band of WZ InGaAs are well resolved, which also indicates that the minimum conduction band in WZ InGaAs must have Γ_7 symmetry.

We also observed from Figure 5a that the energy separation between the lowest absorption band from the PLE spectrum and the PL peak, the so-called Stokes shift, is relatively large, ~35 meV, indicating a different nature of the processes responsible for emission and absorption. In fact, the first absorption edge occurs at the same energy of the high-energy emission observed by μ-PL measurement under higher excitation power density (Figure 4) that was attributed to the excitonic recombination on WZ $In_xGa_{1-x}As$. Meanwhile, the quantum confinement effect is not expected to contribute to the separation since the diameter of the NN is much larger than its Bohr radius. Therefore, we attribute this ~35 meV separation to a Stokes shift. A similar Stokes shift (in the range between 35 and 55 meV) was observed for all measured NNs from this sample and also from the NNs with lower indium composition, as shown from the PL (solid lines) and PLE (dotted lines and symbols) spectra in Figure 5b.

From Figure 5b, it can be clearly seen that the PL emission shifts to higher energies as the indium composition x decreases from 0.20 to 0.12. Correspondingly, the same applies for the absorption line associated with the A band (excitonic peak) in the PLE spectra. The measured energies of the absorption edges and their energy separation are summarized in Table 1. For each indium composition, three different NNs were measured. The parameters in the table are the average values of the measured NNs for each indium composition. As mentioned above, a Stokes shift in the range of 35 to 55 meV is found for all of the measured NNs with different indium composition. The obtained splitting energies between A and B bands (E_{AB}) are approximately 95 meV for the samples with x = 0.20 and x = 0.16. For the sample with x = 0.12, it is worth noticing that the position of the B band is in the energy range where a significant absorption in the GaAs shell occurs. This leads to a strong decrease of the PLE signal from the $In_xGa_{1-x}As$ core, making it difficult to resolve the position of the B band.

To summarize the findings of the bandgap energy, we plot in Figure 6 the E_A for the investigated WZ $In_xGa_{1-x}As$ NN samples as a function of indium composition x. For the ZB $In_xGa_{1-x}As$, we utilize the general interpolation formula (bandgap vs indium composition) from ref 41 to determine the bandgap energy ($E_{g\text{-}ZB}$):

$$E_{g\text{-}ZB}(In_xGa_{1-x}As) = 0.422 + 0.7(1-x) + 0.4(1-x)^2 \text{ at 2K (in eV)}$$

For comparison, the expected data are also plotted in Figure 6. Here, we neglect the bandgap difference between 2 and 10 K. As can be seen, the E_A energies of

all three $In_xGa_{1-x}As$ NN samples are 30−60 meV higher than the respective $E_{g\text{-}ZB}$ values, indicating the blue shift of the bandgap in WZ $In_xGa_{1-x}As$. Meanwhile, the shift exhibits an increasing tendency with the increasing indium composition. As mentioned previously, no theoretical investigations about the band structure of WZ ternary InGaAs have been reported so far. However, for WZ binary alloys InAs and GaAs, many efforts have been done to study their band parameters. De *et al.*[9] and Zanolli *et al.*[8] calculated that the low-temperature bandgap energy of WZ phase InAs is about 55−61 meV higher than the bandgap value of bulk ZB InAs. On the other hand, the experimentally determined bandgap of WZ GaAs is slightly higher (2−8 meV) than the corresponding ZB counterpart at 10 K.[25,29,30] Therefore, for the composition-tunable WZ phase InGaAs the expected bandgap energy difference from the ZB InGaAs should be somewhere within the range of 2−61 meV, depending on composition. This is in good agreement with the range of blue shift as observed experimentally in our study on WZ InGaAs NNs. Moreover, the increasing shift with the increasing indium composition is also consistent with the bandgap difference of WZ GaAs and InAs from their ZB counterpart, respectively.

CONCLUSION

In summary, we have measured PL and PLE spectra for single wurtzite InGaAs−GaAs core−shell NNs. The effective indium composition was determined by polarization-dependent Raman spectroscopy. We deduce a Stokes shift from the energy separation between PL and PLE spectra. The experimental results for the valence band-splitting energies of composition-tunable InGaAs NNs in the wurtizte phase were presented. These parameters have never been reported before. They are, however, fundamental for the optical properties of InGaAs NNs and, therefore, of considerable interest to the development of nanoscale device applications based on these structures.

EXPERIMENTAL SECTION

Nanoneedle Growth. WZ $In_xGa_{1-x}As$ NNs were grown by MOCVD at 76 Torr and 400−420 °C on Si substrates for 60 min, resulting in ~3 μm long NNs with ~600 nm wide bases. The metal−organic precursors were trimethylindium, triethylgallium, and tertiarybutylarsine. Details of the growth procedure are described in refs 24, 42, and 43. The growth assumes a core−shell growth mechanism in which the axial and radial growths occur simultaneously. However, the vertical growth saturates when the NN length reaches ~2 μm while the radial growth continues. This turns the originally sharp needles into blunt pillars. At the end of the growth process, a WZ GaAs shell is grown to passivate the NN surface. The thickness of the GaAs capping layer is 30 nm for all samples with indium composition of 0.12, 0.16, and 0.20.

Characterization. We performed polarization-dependent Raman measurements on single NNs in order to determine the effective indium composition and the symmetries of the vibrational modes, which reflect the symmetry of the crystals. Raman spectra were collected at room temperature in backscattering geometry using a 100× objective (NA = 0.95) with the 514.5 nm line of an Ar^+ laser (E_L = 2.41 eV) as excitation. The scattered light was collected by an XY Dilor triple spectrometer equipped with a multichannel charge coupled device (CCD) detector and with a spectral resolution of about 1 cm^{-1}. For polarization-dependent measurements, the polarization of the excitation was rotated through a $\lambda/2$ plate. A linear polarizer was used to analyze the polarization of the scattered light.

We performed PL and PLE measurements on single $In_xGa_{1-x}As$ NNs in a cryogenic confocal microscope system (Attocube[44]) at a temperature of 10 K. As an excitation source we used a He−Ne laser at 1.96 eV for PL measurements and two continuously tunable Ti:sapphire lasers in different spectral ranges, thus covering the entire range between 1.28 and 1.63 eV for PLE measurements. The laser light was focused with an objective of NA = 0.62 down to a spot of ~1 μm diameter, and the emission was collected through the same objective. For PL, the signal was sent to a 0.5 m focal length spectrograph equipped with 1200 grooves/mm grating followed by a liquid nitrogen cooled silicon CCD detector. In the case of PLE experiments, the emission was spectrally analyzed by a 0.5 m focal length double spectrometer. During the PLE measurement, a set of neutral density filters and laser power meter were used to calibrate the intensity of the incident excitation power at each wavelength. To address individual NN by μ-PL spectroscopy, NNs were mechanically transferred from their growth substrates to patterned silicon substrates so that the same NN could be easily identified for repeated optical measurements.

Conflict of Interest: The authors declare no competing financial interest.

Acknowledgment. We kindly thank V. Jovanov and S. Funk for their experimental help. This work was supported financially by the DFG via the excellence cluster Nanosystems Initiative Munich (NIM), the collaborative research center SFB 631, DoD NSSEFF Fellowship (N00244-09-1-0013 and N00244-09-1-0080), and the Center for Energy Efficient Electronics Science (NSF Award 0939514). We acknowledge support of the National Center for Electron Microscopy, LBL, which is supported by the U.S. DOE (DE-AC02-05CH11231). X.W. acknowledges support from the European Union Erasmus Mundus TANDEM program and the National Natural Science Foundation of China (11304228).

REFERENCES AND NOTES

1. McMahon, M. I.; Nelmes, R. J. Observation of a Wurtzite Form of Gallium Arsenide. *Phys. Rev. Lett.* **2005**, *95*, 215505.
2. Akiyama, T.; Sano, K.; Nakamura, K.; Ito, T. An Empirical Potential Approach to Wurtzite-Zinc-Blende Polytypism in Group III-V Semiconductor Nanowires. *Jpn. J. Appl. Phys.* **2006**, *45*, L275–L278.
3. Glas, F.; Harmand, J.-C.; Patriarche, G. Why Does Wurtzite Form in Nanowires of III-V Zinc Blende Semiconductors? *Phys. Rev. Lett.* **2007**, *99*, 146101.
4. Caroff, P.; Dick, K. A.; Johansson, J.; Messing, M. E.; Deppert, K.; Samuelson, L. Controlled Polytypic and Twin-Plane Superlattices in III-V Nanowires. *Nat. Nano.* **2009**, *4*, 50–55.
5. Dick, K. A.; Caroff, P.; Bolinsson, J.; Messing, M. E.; Johansson, J.; Deppert, K.; Wallenberg, L. R.; Samuelson, L. Control of III-V Nanowire Crystal Structure by Growth Parameter Tuning. *Semicond. Sci. Technol.* **2010**, *25*, 024009.
6. Johansson, J.; Bolinsson, J.; Ek, M.; Caroff, P.; Dick, K. A. Combinatorial Approaches to Understanding Polytypism in III-V Nanowires. *ACS Nano* **2012**, *6*, 6142–6149.
7. Zhang, L.; Luo, J.-W.; Zunger, A.; Akopian, N.; Zwiller, V.; Harmand, J.-C. Wide InP Nanowires with Wurtzite/Zincblende Superlattice Segments Are Type-II Whereas Narrower Nanowires Become Type-I: An Atomistic

Pseudopotential Calculation. *Nano Lett.* **2010**, *10*, 4055–4060.
8. Zanolli, Z.; Fuchs, F.; Furthmüller, J.; von Barth, U.; Bechstedt, F. Model GW Band Structure of InAs and GaAs in the Wurtzite Phase. *Phys. Rev. B* **2007**, *75*, 245121.
9. De, A.; Pryor, C. E. Predicted Band Structures of III-V Semiconductors in the Wurtzite Phase. *Phys. Rev. B* **2010**, *81*, 155210.
10. Belabbes, A.; Panse, C.; Furthmüller, J.; Bechstedt, F. Electronic Bands of III-V Semiconductor Polytypes and Their Alignment. *Phys. Rev. B* **2012**, *86*, 075208.
11. Perera, S.; Pemasiri, K.; Fickenscher, M. A.; Jackson, H. E.; Smith, L. M.; Yarrison-Rice, J.; Paiman, S.; Gao, Q.; Tan, H. H.; Jagadish, C. Probing Valence Band Structure in Wurtzite InP Nanowires Using Excitation Spectroscopy. *Appl. Phys. Lett.* **2010**, *97*, 023106.
12. Gadret, E. G.; Dias, G. O.; Dacal, L. C. O.; de Lima, M. M., Jr.; Ruffo, C. V. R. S.; Iikawa, F.; Brasil, M. J. S. P.; Chiaramonte, T.; Cotta, M. A.; Tizei, L. H. G.; *et al.* Valence-Band Splitting Energies in Wurtzite InP Nanowires: Photoluminescence Spectroscopy and Ab Initio Calculations. *Phys. Rev. B* **2010**, *82*, 125327.
13. Tuin, G.; Borgström, M.; Trägårdh, J.; Ek, M.; Wallenberg, L. R.; Samuelson, L.; Pistol, M.-E. Valence Band Splitting in Wurtzite InP Nanowires Observed by Photoluminescence and Photoluminescence Excitation Spectroscopy. *Nano Res.* **2011**, *4*, 159–163.
14. Montazeri, M.; Wade, A.; Fickenscher, M.; Jackson, H. E.; Smith, L. M.; Yarrison-Rice, J. M.; Gao, Q.; Tan, H. H.; Jagadish, C. Photomodulated Rayleigh Scattering of Single Semiconductor Nanowires: Probing Electronic Band Structure. *Nano Lett.* **2011**, *11*, 4329–4336.
15. Perera, S.; Shi, T.; Fickenscher, M. A.; Jackson, H. E.; Smith, L. M.; Yarrison-Rice, J. M.; Paiman, S.; Gao, Q.; Tan, H. H.; Jagadish, C. Illuminating the Second Conduction Band and Spin-Orbit Energy in Single Wurtzite InP Nanowires. *Nano Lett.* **2013**, *13*, 5367–5372.
16. Morkötter, S.; Funk, S.; Liang, M.; Döblinger, M.; Hertenberger, S.; Treu, J.; Rudolph, D.; Yadav, A.; Becker, J.; Bichler, M.; *et al.* Role of Microstructure on Optical Properties in High-Uniformity $In_{1-x}Ga_xAs$ Nanowire Arrays: Evidence of a Wider Wurtzite Band Gap. *Phys. Rev. B* **2013**, *87*, 205303.
17. Koblmüller, G.; Abstreiter, G. Growth and Properties of InGaAs Nanowires on Silicon. *Phys. Status Solidi RRL* **2014**, *8*, 11–30.
18. Shin, J. C.; Kim, K. H.; Yu, K. J.; Hu, H.; Yin, L.; Ning, C.-Z.; Rogers, J. A.; Zuo, J.-M.; Li, X. $In_xGa_{1-x}As$ Nanowires on Silicon: One-Dimensional Heterogeneous Epitaxy, Bandgap Engineering, and Photovoltaics. *Nano Lett.* **2011**, *11*, 4831–4838.
19. Chen, R.; Tran, T.-T. D.; Ng, K. W.; Ko, W. S.; Chuang, L. C.; Sedgwick, F. G.; Chang-Hasnain, C. Nanolasers Grown on Silicon. *Nat. Photonics* **2011**, *5*, 170–175.
20. Lu, F.; Tran, T.-T. D.; Ko, W. S.; Ng, K. W.; Chen, R.; Chang-Hasnain, C. Nanolasers Grown on Silicon-Based MOSFETs. *Opt. Express* **2012**, *20*, 12171–12176.
21. Li, K.; Sun, H.; Ren, F.; Ng, K. W.; Tran, T.-T. D.; Chen, R.; Chang-Hasnain, C. J. Tailoring the Optical Characteristics of Microsized InP Nanoneedles Directly Grown on Silicon. *Nano Lett.* **2013**, *14*, 183–190.
22. Yang, T.; Hertenberger, S.; Morkötter, S.; Abstreiter, G.; Koblmüller, G. Size, Composition, and Doping Effects on In(Ga)As Nanowire/Si Tunnel Diodes Probed by Conductive Atomic Force Microscopy. *Appl. Phys. Lett.* **2012**, *101*, 233102.
23. Tomioka, K.; Yoshimura, M.; Fukui, T. A III-V Nanowire Channel on Silicon for High-Performance Vertical Transistors. *Nature* **2012**, *488*, 189–192.
24. Moewe, M.; Chuang, L. C.; Crankshaw, S.; Ng, K. W.; Chang-Hasnain, C. Core-Shell InGaAs/GaAs Quantum Well Nanoneedles Grown on Silicon with Silicon-Transparent Emission. *Opt. Express* **2009**, *17*, 7831–7836.
25. Ketterer, B.; Heiss, M.; Uccelli, E.; Arbiol, J. Fontcuberta i Morral, A. Untangling the Electronic Band Structure of Wurtzite GaAs Nanowires by Resonant Raman Spectroscopy. *ACS Nano* **2011**, *5*, 7585–7592.
26. Ahtapodov, L.; Todorovic, J.; Olk, P.; Mjåland, T.; Slåttnes, P.; Dheeraj, D. L.; van Helvoort, A. T. J.; Fimland, B.-O.; Weman, H. A Story Told by a Single Nanowire: Optical Properties of Wurtzite GaAs. *Nano Lett.* **2012**, *12*, 6090–6095.
27. Kusch, P.; Breuer, S.; Ramsteiner, M.; Geelhaar, L.; Riechert, H.; Reich, S. Band Gap of Wurtzite GaAs: A Resonant Raman Study. *Phys. Rev. B* **2012**, *86*, 075317.
28. Peng, W.; Jabeen, F.; Jusserand, B.; Harmand, J. C.; Bernard, M. Conduction Band Structure in Wurtzite GaAs Nanowires: A Resonant Raman Scattering Study. *Appl. Phys. Lett.* **2012**, *100*, 073102.
29. De Luca, M.; Lavenuta, G.; Polimeni, A.; Rubini, S.; Grillo, V.; Mura, F.; Miriametro, A.; Capizzi, M.; Martelli, F. Excitonic Recombination and Absorption in $In_xGa_{1-x}As$/GaAs Heterostructure Nanowires. *Phys. Rev. B* **2013**, *87*, 235304.
30. De Luca, M.; Polimeni, A.; Felici, M.; Miriametro, A.; Capizzi, M.; Mura, F.; Rubini, S.; Martelli, F. Resonant Depletion of Photogenerated Carriers in InGaAs/GaAs Nanowire Mats. *Appl. Phys. Lett.* **2013**, *102*, 173102.
31. Zardo, I.; Yazji, S.; Hörmann, N.; Hertenberger, S.; Funk, S.; Mangialardo, S.; Morkötter, S.; Koblmüller, G.; Postorino, P.; Abstreiter, G. E_1(A) Electronic Band Gap in Wurtzite InAs Nanowires Studied by Resonant Raman Scattering. *Nano Lett.* **2013**, *13*, 3011–3016.
32. Yu, P. Y.; Cardona, M. *Fundamentals of Semiconductors*, 4th ed.; Springer-Verlag: Berlin, 2010.
33. Pearsall, T. P.; Carles, R.; Portal, J. C. Single Longitudinal-Mode Optical Phonon Scattering in $Ga_{0.47}In_{0.53}As$. *Appl. Phys. Lett.* **1983**, *42*, 436–438.
34. Goetz, K.-H.; Bimberg, D.; Jürgensen, H.; Selders, J.; Solomonov, A. V.; Glinskii, G. F.; Razeghi, M. Optical and Crystallographic Properties and Impurity Incorporation of $Ga_xIn_{1-x}As$ ($0.44 < x<0.49$) Grown by Liquid Phase Epitaxy, Vapor Phase Epitaxy, and Metal Organic Chemical Vapor Deposition. *J. Appl. Phys.* **1983**, *54*, 4543–4552.
35. Miller, R. C.; Kleinman, D. A.; Tsang, W. T.; Gossard, A. C. Observation of the Excited Level of Excitons in GaAs Quantum Wells. *Phys. Rev. B* **1981**, *24*, 1134–1136.
36. Miller, R. C.; Gossard, A. C.; Tsang, W. T.; Munteanu, O. Extrinsic Photoluminescence from GaAs Quantum Wells. *Phys. Rev. B* **1982**, *25*, 3871–3877.
37. Ilouz, I.; Oiknine-Schlesinger, J.; Gershoni, D.; Ehrenfreund, E.; Ritter, D.; Hamm, R. A.; Vandenberg, J. M. Optical Transitions Between Light Hole Subbands in InGaAs/InP Strained Layer Multiquantum Wells. *Appl. Phys. Lett.* **1995**, *66*, 2268–2270.
38. Yu, P. W. Excitation-Dependent Emission in Mg-, Be-, Cd-, and Zn-Implanted GaAs. *J. Appl. Phys.* **1977**, *48*, 5043–5051.
39. Wang, L. S.; Fong, W. K.; Surya, C.; Cheah, K. W.; Zheng, W. H.; Wang, Z. G. Photoluminescence of Rapid-Thermal Annealed Mg-Doped GaN Films. *Solid-State Electron.* **2001**, *45*, 1153–1157.
40. Signorello, G.; Lörtscher, E.; Khomyakov, P. A.; Karg, S.; Dheeraj, D. L.; Gotsmann, B.; Weman, H.; Riel, H. Inducing a Direct-to-Pseudodirect Bandgap Transition in Wurtzite GaAs Nanowires with Uniaxial Stress. *Nat. Commun.* **2014**, *5*, 3655.
41. Chuang, S. L. *Physics of Optoelectronic Devices*, 2nd ed.; John Wiley & Sons, Inc.: New York, 2009.
42. Moewe, M.; Chuang, L. C.; Crankshaw, S.; Chase, C.; Chang-Hasnain, C. Atomically Sharp Catalyst-Free Wurtzite GaAs/AlGaAs Nanoneedles Grown on Silicon. *Appl. Phys. Lett.* **2008**, *93*, 023116.
43. Ng, K. W.; Ko, W. S.; Tran, T.-T. D.; Chen, R.; Nazarenko, M. V.; Lu, F.; Dubrovskii, V. G.; Kamp, M.; Forchel, A.; Chang-Hasnain, C. J. Unconventional Growth Mechanism for Monolithic Integration of III-V on Silicon. *ACS Nano* **2012**, *7*, 100–107.
44. http://www.attocube.com. Accessed on Oct 31, 2014.